Appl. Phys. A (2016) 122:101
DOI 10.1007/s00339-016-9639-0

Applied Physics A
Materials Science & Processing

Effect of Si addition on the structure and corrosion behavior of NbN thin films deposited by unbalanced magnetron sputtering

L. Velasco[1,2] · J. J. Olaya[1] · S. E. Rodil[3]

Received: 22 November 2015 / Accepted: 15 January 2016 / Published online: 28 January 2016

Abstract In this work, nanostructured $Nb_xSi_yN_z$ thin films were deposited onto stainless steel AISI 304 substrates by co-sputtering a Nb target with Si additions while using unbalanced magnetron sputtering. The microstructure was analyzed by X-ray diffraction, and the chemical composition was identified by X-ray photoelectron spectroscopy. The hardness was measured by nanoindentation, and the corrosion resistance was studied by potentiodynamic polarization curves and electrochemical impedance spectroscopy using a 3 wt% NaCl solution. The addition of Si in the NbN thin films changed the microstructure from a crystalline to an amorphous phase. The chemical analysis showed the presence of both Si_3N_4 and NbN phases. The hardness decreased from 20 GPa (NbN) to 15 GPa for the film with the highest Si concentration (28.6 at.%). Nevertheless, the corrosion properties were significantly improved as the Si concentration increased; the polarization resistance after 168 h of immersion was two orders of magnitude larger in comparison with the substrate.

✉ L. Velasco
leoveles@gmail.com; lvelascoe@unal.edu.co

[1] Departamento de Ingeniería Mecánica y Mecatrónica, Facultad de Ingeniería, Universidad Nacional de Colombia, AA 14490 Bogotá, Colombia

[2] Department of Chemical Engineering and Materials Science, University of Southern California, Los Angeles, CA 90089, USA

[3] Instituto de Investigaciones en Materiales, Universidad Nacional Autónoma de México, 04510 Mexico, D. F., Mexico

1 Introduction

The synthesis of superhard nanocomposite coatings has significantly improved the lifetime of cutting tools, molds, and structures [1]. Such films have been deposited by different techniques; physical vapor deposition methods (PVD) have demonstrated good efficiency by improving mechanical, electrical, optical, and chemical properties [2–6]. In particular, the unbalanced magnetron sputtering (UBM) process provides higher deposition rates, a denser structure under low temperatures, and better film-substrate adhesion than balanced magnetron sputtering, which are properties that enhance the lifetime of substrate–thin-film systems [7–9]. A common feature of the nanocomposite coatings is the addition of Si into hard metal nitrides (MeN), such as Cr–Si–N [10–15], Ti–Si–N [16, 17], V–Si–N [18], W–Si–N [19–21], and Nb–Si–N [22–26]. Most of those studies have shown an improvement in the mechanical properties, but few studies have analyzed the effect of the Si-modified structure on the corrosion resistance [27].

In our research group, we have been investigating the corrosion resistance of different coatings for a variety of applications, such as tools or biomedical implants [28–34]. The corrosion resistance of metal nitride coatings TiN, TaN, NbN, and CrN was affected by the energy deposited (degree of bombardment) during the deposition [29, 31, 33, 35–38]; it was shown that highly energetic conditions were generally detrimental for the corrosion resistance, contrary to the behavior observed for the hardness. The lower corrosion protection of the hard films was associated with a higher degree of stress, which induces adhesive failures of the coatings during immersion in the electrolyte. Moreover, it is well known that the corrosion resistance of PVD coatings is controlled by the presence of the intrinsic porosity, which is mainly due to the columnar boundaries

and grain boundaries that result under typical PVD deposition conditions. Therefore, our hypothesis in this work was that the amorphous Si_yN_z-based second phase, which has been extensively used to enhance the film hardness [20, 22, 39], could help to improve the corrosion resistance by reducing the intrinsic porosity, while maintaining a relative high hardness in the films.

Niobium nitride (NbN) coatings have been deposited onto steel substrates using UBM sputtering, providing relative good corrosion resistance and high hardness [33, 37, 38, 40]. Moreover, it has been shown that the addition of Si to NbN can increase the film hardness [22–26]. However, there are no studies on the effect of the Si addition on the corrosion resistance of the films. In this work, $Nb_xSi_yN_z$ films were produced by co-sputtering Nb and Si, where square Si pieces were placed over the racetrack of a Nb target. By increasing the number of Si pieces, it was possible to produce $Nb_xSi_yN_z$ films with different Si concentrations, leading to changes in the microstructure, hardness, and corrosion resistance.

2 Experimental details

Thin $Nb_xSi_yN_z$ films with different Si concentrations were deposited using UBM sputtering from a combined Nb–Si target, where small pieces of Si were added to the surface of the Nb target. The deposition conditions were as follows: working pressure at 6×10^{-1} Pa, Ar (99.99 %) and N_2 (99.99 %) flow rates of 9 and 3 sccm, respectively. The current during the sputtering process was maintained at 350 mA, applied to the 101.6 mm (4″) diameter Nb (99.99 %) target. Figure 1 shows a schematic of the distribution of the 7 × 7 mm Si pieces (purity 99.999 %) on top of the Nb target. In order to maintain the uniformity of the film composition, the substrates were rotated at 35 rpm. Two substrates were used: Si (100) to measure the deposition rate and stainless steel (AISI 304) substrate disks (14 mm × 2 mm) for the electrochemical and structural characterization. The steel disks were mirror-polished using an alumina solution to obtain a final roughness of ~4 nm. After polishing, the substrates were ultrasonically cleaned with acetone and isopropyl alcohol for 5 min each.

In order to improve the adhesion between the substrate and the $Nb_xSi_yN_z$ films, a thin layer (~100 nm) of Nb_xSi_y was deposited onto the substrates prior to the introduction of N_2 inside the chamber. The deposition time was adjusted according to the deposition rate previously determined for NbN to obtain films with thicknesses of ~1000 nm (20 min). The final thicknesses and deposition rates were determined using a profilometer (DEKTAK 150) measuring a step along a displacement of 200 μm and an applied force of 1 mg. X-ray diffraction (XRD) patterns were obtained using a Cu Kα radiation source at 45 kV and 40 mA in an Xpert-Pro Panalytical device in the Bragg–Brentano mode. The morphology of the coatings was characterized by scanning electron microscopy (SEM) using a FEI QUANTA 200 SEM. The chemical composition was determined by X-ray photoelectron spectroscopy (XPS) (VG Scientific Multilab ESCA 2000), the XPS was operated at 8×10^{-7} Pa using Al Kα radiation $hv = 1486.6$ eV with a spatial resolution of 500 μm and 50 and 20 eV pass energy to acquire the survey and high-resolution spectra, respectively. The spectra analyzed here were obtained without Ar cleaning, since the N1s signal was strongly decreased by the Ar bombardment and oxygen was actually found bonded to niobium. High-resolution spectra were acquired for Nb 3d, N 1s, and Si 2p photoelectron peak energy regions. The XPS error is based on a detection limit estimated to be about 1 % and proper propagation of uncertainties. The hardness was measured with a nanohardness tester (CSM) using a Berkovich triangular pyramid indenter and a peak load of 5 mN.

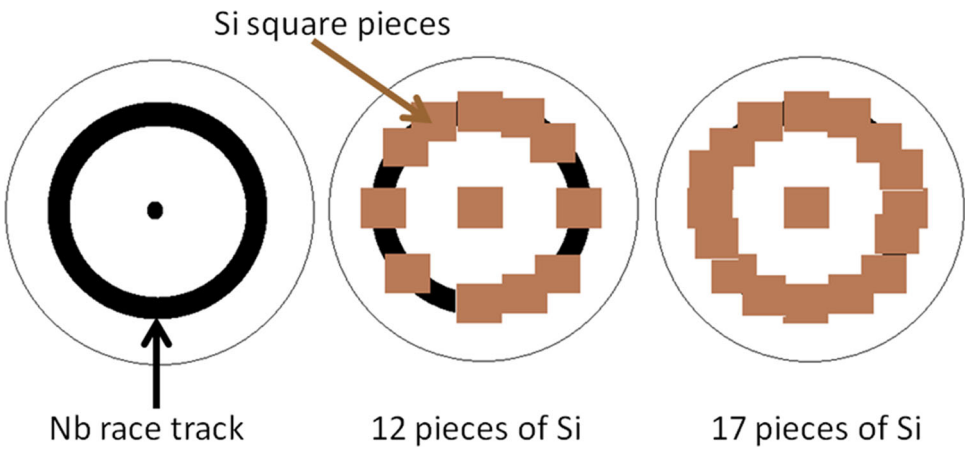

Fig. 1 A graphical representation of the distribution of the Si pieces on the Nb target is shown for each condition, where the *black line* indicates the target race track

The corrosion and electrochemical behaviors of the uncoated and coated specimens were studied using a three-electrode system and a Gamry 600 potentiostat at room temperature. The samples were mounted in a special cell which limited the exposed area of the coated steel substrate face to be 0.196 cm^2. In the corrosion resistance experiments, the substrates were placed as the working electrode, a carbon rod was used as the counter electrode, a saturated calomel electrode was used as the reference electrode, and a 3 wt% NaCl solution was used as the electrolyte (pH 7.9). Prior to each corrosion experiment, the corrosion potential was allowed to stabilize during a 0.5-h immersion in the test solution, followed by the conduction of potentiodynamic polarization (PP) or electrochemical impedance tests. In the PP experiments, the initial potential was 500 mV below the open-circuit potential and the scanning rate was 1 mV/s, The corrosion current density (I_{corr}) was estimated by a linear fit and Taffel extrapolation to the cathodic part of the polarization curve. Afterward, the specimens were examined by SEM to detect surface pitting. Electrochemical impedance spectroscopy (EIS) measurements were taken using the same custom cell described above at a stable open-circuit potential. The perturbing signal had an AC amplitude of 10 mV and frequency range from 0.01 Hz to 100 kHz. Measurements were taken after 1, 2, 24, 48, and 168 h of immersion. The analysis of the EIS was conducted using the equivalent circuit fitting model in the Gamry Echem Analyst software.

3 Results and discussion

Table 1 shows the physical properties of the samples as a function of the number of Si pieces added to the Nb target. The table includes the chemical composition obtained by XPS, the approximate grain size, the hardness, and the Young's Modulus.

The chemical composition analysis for the samples conducted by XPS is presented in Fig. 2. Low-resolution XPS survey spectra for each of the samples are displayed in Fig. 2a, while in Fig. 2b–d high-resolution XPS spectra for the N 1s, Si 2p, and Nb 3p peaks are displayed. The analysis of the N 1s peak shows that it can be deconvoluted into two peaks (except for the sample where no Si pieces were placed on top of the target), and the binding energies for the two peaks are 397.4 eV and 398.8 eV, which are attributed to Si_3N_4 and NbN, respectively [41, 42]. As shown in Table 1, the N concentration remained relatively constant, which suggests that nitrides were formed in all the experiments. Meanwhile, the intensity of the Si 2p peaks increased as the number of Si pieces on top of the Nb target increased. The high-resolution spectrum for Si 2p in Fig. 2c shows only a single peak at 101.7 eV, which is attributed to Si atoms bonded to N (Si_3N_4) [43, 44]. There is no evidence of pure Si, which should be at 99.1 eV, or silicon oxide (SiO_2) at 103.4 eV. On the other hand, there is a large variation in the Nb 3d signal as the Si content was increased (Fig. 2d); the Nb 3d doublet is very clear for the sample with 0 at.% Si. However, the Nb 3d relative peak intensity decreases as the concentration of Si increases, and the Nb 3d doublet becomes less defined for the sample with the highest Si concentration. Oxygen was found to be bonded to Nb, and the deconvolution of the Nb 3d signal revealed the presence of two double peaks: NbN and Nb_2O_5. The presence of oxygen could explain the low film hardness as will be presented later. The message from the XPS analysis is the existence of both NbN and Si_3N_4 phases in all the Si-doped thin films, as has been found in similar studies [22–24, 45–47].

To confirm our interpretation of the XPS analysis, in Fig. 3, XRD patterns are displayed as a function of the Si concentration. It can be observed that for the sample with 0 at.% Si two characteristics peaks appeared, at 34.66° and 40.83°, which correspond to the cubic NbN phase (PDF database 0-071-0162). Another peak appeared at 37.02°, which belongs to the 100-nm Nb_xSi_y interlayer that was co-deposited to enhance the adhesion between the substrate and the film (PDF database 01-088-2330). The other peaks observed in Fig. 3 correspond to the stainless steel 304 (SS 304) substrate. By using the Scherrer equation [48], the NbN crystalline size was estimated (Table 1) for each of the samples; the crystalline size dramatically decreased as the Si content was increased from 0 (19.3 nm) to 13.1 at.% Si (2.3 nm). Further increase in the Si content led to a completely amorphous coating, as is shown for the 28.6 at.% Si XRD pattern, where the NbN peaks are not

Table 1 Physical properties of the samples, chemical composition, estimated grain size, hardness, and Young's modulus

Sample name	Silicon pieces	Nitrogen (at.%)	Niobium (at.%)	Silicon (at.%)	Crystalline size (nm)	Hardness (GPa)	Young modulus (GPa)
NbN-0Si	0	37.1	45.3	0	~19	21.6 ± 1.2	232 ± 7
NbN-12Si	12	41.5	32.2	13.1	~3	19.9 ± 1.2	185 ± 2
NbN-17Si	17	39.9	13.2	28.6	Amorphous	14.9 ± 0.9	155 ± 7

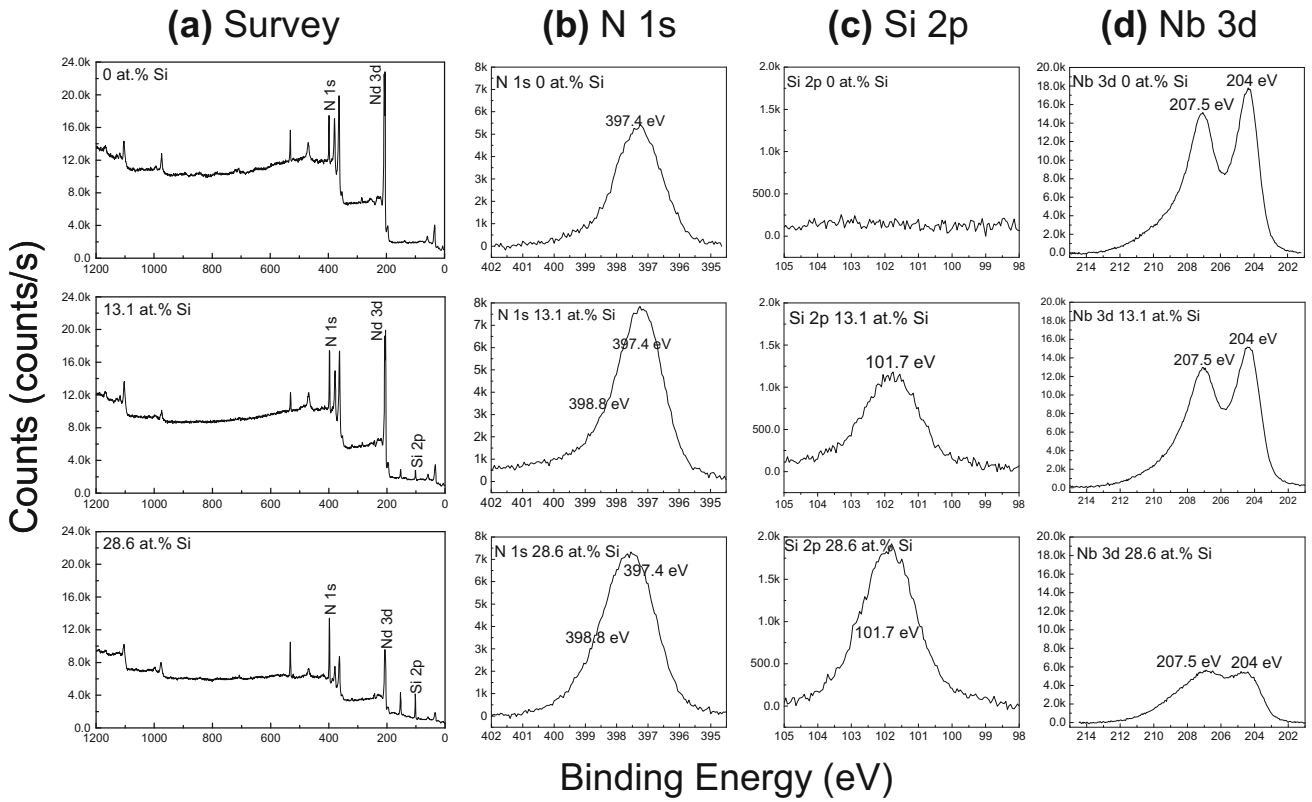

Fig. 2 Chemical composition analysis for the samples conducted by XPS. **a** Low-resolution XPS survey spectra for the films with different content of Si. **b–d** are high-resolution XPS spectra for Nb 3d, Si 2p, and N 1s peaks for the different Si concentrations, respectively

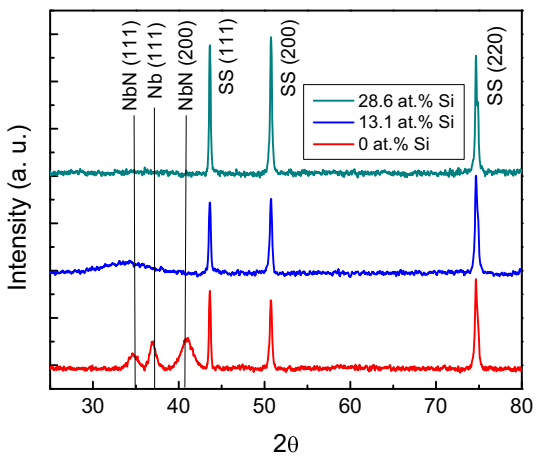

Fig. 3 Normalized XRD patterns for various Si concentrations. The NbN peaks disappeared as the Si content in the films increased

present. Evidence of crystalline Si_3N_4 was not found for any of the samples, which suggests that the Si_3N_4 phase observed by XPS is mainly amorphous, as described by other authors [10, 18, 41, 46, 49]. The amorphous Si_3N_4 (a-Si_3N_4) phase may be surrounding the NbN nanograins, thus limiting their growth [22, 23, 45–47, 50]. However, no direct evidence of such structural change can be inferred from the present results. Furthermore, the deposition method was not precise enough to incorporate Si at smaller percentages, so we observed a sharp crystalline-amorphous phase transition. Nevertheless, as shown later, the corrosion resistance of the amorphous coatings was significantly enhanced.

The hardness and Young's Modulus values, presented in Table 1, decreased as the Si content was increased, and the sample with 0 at.% Si presented the highest hardness and Young's modulus. However, the values obtained were lower than those usually reported for NbN, which can be associated with the oxygen contamination. As the Si content was increased, the reduction in hardness is attributed to the a-Si_3N_4 phase. It has been reported than when the a-Si_3N_4 layer is larger than the grain size of the NbN phase, a different deformation mechanism can operate: grain sliding. This mechanism can be activated when the distance between the NbN nanograins is larger than their size and would result in a decrease in hardness and Young's Modulus [47]. Nevertheless, the hardness achieved for the film with the highest Si content is $\sim$5 times higher than that of the SS 304 ($\sim$3 GPa) [51].

Regarding the electrochemical characterization, Fig. 4 shows the open-circuit potential (OCP) acquired as a function of time in the 3 wt% NaCl solution. Different

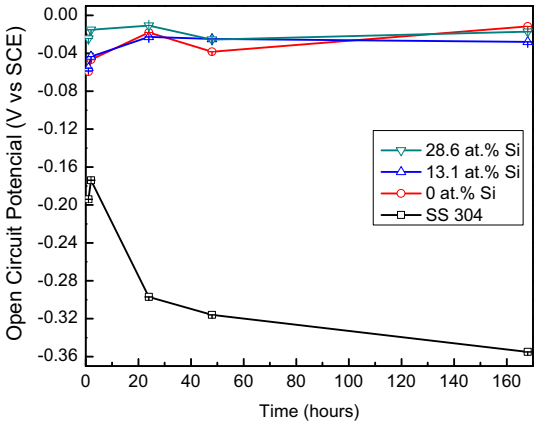

Fig. 4 Open-circuit potential (OCP) as a function of the immersion time. The OCP for the SS 304 decreased as the immersion time increased, while for the coated substrates the OCP remained constant

corrosion processes occur for the coated and the uncoated SS 304 specimens, and it can be observed that the OCP is in the −100 to −4 mV range for the coated substrates, being relatively stable or becoming more positive as time goes on. Meanwhile, for the uncoated SS 304 substrate, the OCP becomes more negative with time, reaching an equilibrium value of −355 mV after 168 h of immersion. Overall, no strong differences were observed as a function of the Si content, except for the initial times, where the film with the highest Si content presented slightly higher OCP values.

Typical potentiodynamic polarization curves obtained from the coated and uncoated SS 304 specimens are presented in Fig. 5. Here, it is clear that the coated specimens presented better corrosion resistance than the uncoated SS 304 (the curves are shifted to the left-upper part of the plot); specifically, the sample with the highest Si content

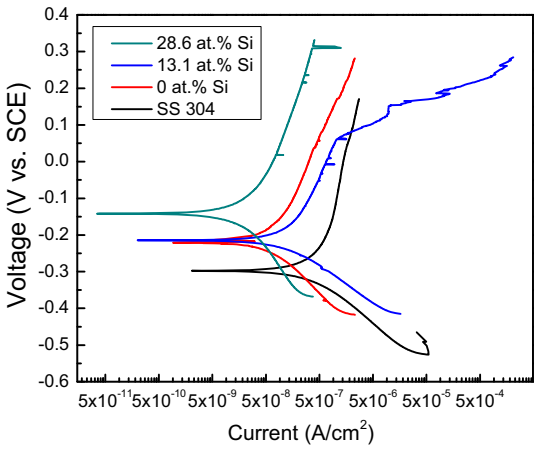

Fig. 5 Potentiodynamic polarization curves obtained after the 168 h of immersion for the films and SS 304. The corrosion current decreases as the Si content in the films increases

showed the lowest corrosion current density (I_{corr}). The results from the Tafel analysis are shown in Table 2, where there is a decrease in the I_{corr} from 184 nA/cm^2 for the SS 304 to 23 nA/cm^2 for the 28.6 at.% Si sample. Since I_{corr} is directly proportional to the corrosion rate of a sample, this indicates that improved corrosion resistance is provided by the coatings.

The improved corrosion resistance and stability of the coatings when immersed in the electrolyte are shown by the EIS data as a function of the immersion time. Figure 6 compares the evolution in time of the impedance spectra of the SS 304 and the coated specimens. Figure 6a, c, e, g shows that the impedance modulus (Zmod) is one order of magnitude larger for the films than the SS 304 and that there are no significant changes in Zmod as the immersion time increases for the films, while in the SS 304 Zmod decreased after the first 2 h of immersion time. In Fig. 6b, d, f, h, it is shown that the phase angle of the films remained stable during 168 h of immersion, while the SS 304 relaxation time decreased after the first 2 h of immersion. A summary of these results is presented in Fig. 7, where only the impedance spectra for each of the samples after an immersion time of 168 h are displayed. Figure 7a shows a linear relationship between the log of Zmod and the log of frequency in the coated specimens, which is symptomatic of a predominantly capacitive behavior at the electrode/solution interface. Moreover, at lower frequencies there is an increase in the impedance (from 10^5 Ω to 2×10^6 Ω) as the Si content increases, where the film with the highest Si concentration showed the highest Zmod, while for the SS 304 at higher frequencies Zmod is at least one order of magnitude lower than for the coated substrates. The phase angle for the $Nb_xSi_yN_z$ thin films is higher than the one observed for the SS 304 sample (Fig. 7b) and shows a long relaxation time, which can be correlated with the $Nb_xSi_yN_z$ dielectric properties. In the frequency range of 10^{-2}–10^2 Hz, the phase angle has values close to 80° which is characteristic of an extended relaxation time, while at high frequencies the phase angle shift is close to 0 and an ohmic resistance dominates the system impedance. The long relaxation time reveals a capacitive behavior, which is indicative of a high passivation degree of the microporosities that are usually

Table 2 Results from Tafel extrapolation, corrosion current density, and corrosion potential for each sample

Sample name	Silicon (at.%)	I_{corr} (nA/cm^2)	E_{corr} (mV)
SS 304	0	184 ± 8	−272 ± 36
NbN-0Si	0	110 ± 4	−187 ± 35
NbN-12Si	13.1	148 ± 7	−231 ± 14
NbN-17Si	28.6	23 ± 18	−176 ± 47

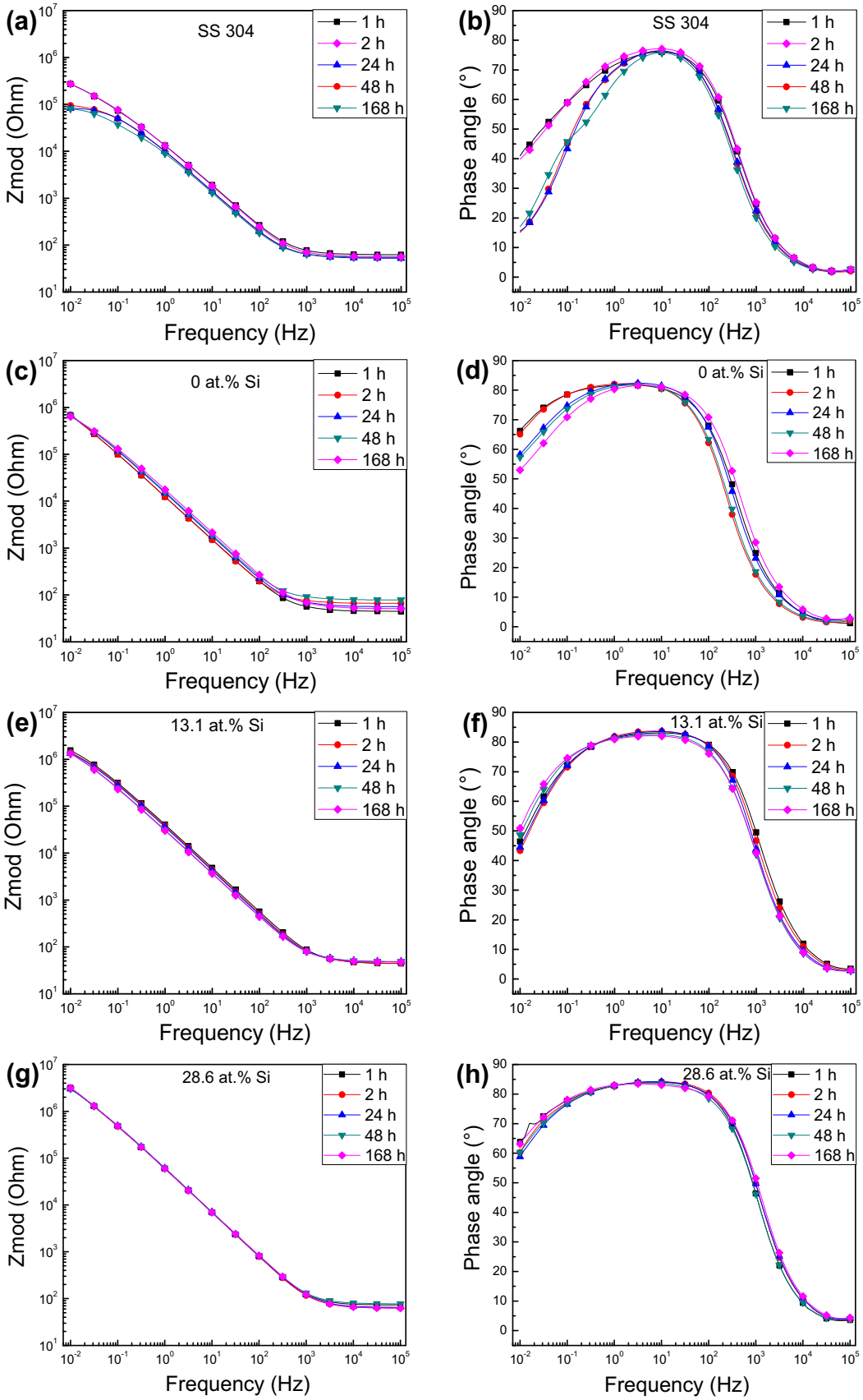
(a)
SS 304
Zmod (Ohm)
Frequency (Hz)
(b)
SS 304
Phase angle (°)
Frequency (Hz)
(c)
0 at.% Si
Zmod (Ohm)
Frequency (Hz)
(d)
0 at.% Si
Phase angle (°)
Frequency (Hz)
(e)
13.1 at.% Si
Zmod (Ohm)
Frequency (Hz)
(f)
13.1 at.% Si
Phase angle (°)
Frequency (Hz)
(g)
28.6 at.% Si
Zmod (Ohm)
Frequency (Hz)
(h)
28.6 at.% Si
Phase angle (°)
Frequency (Hz)
1 h
2 h
24 h
48 h
168 h

◀**Fig. 6** Evolution in time of the impedance spectra. Impedance modulus (Zmod) for: **a** SS 304 substrate, **c** film with 0 at.% Si, **e** film with 13.1 at.% Si, and **g** film with 28.6 at.% Si. Phase angle for: **b** SS 304 substrate, **d** film with 0 at.% Si, **f** film with 13.1 at.% Si, and **h** film with 28.6 at.% Si. The impedance modulus (Zmod) was one order of magnitude larger for the films than for the SS 304. The phase angles remained stable for the films in comparison with the SS 304

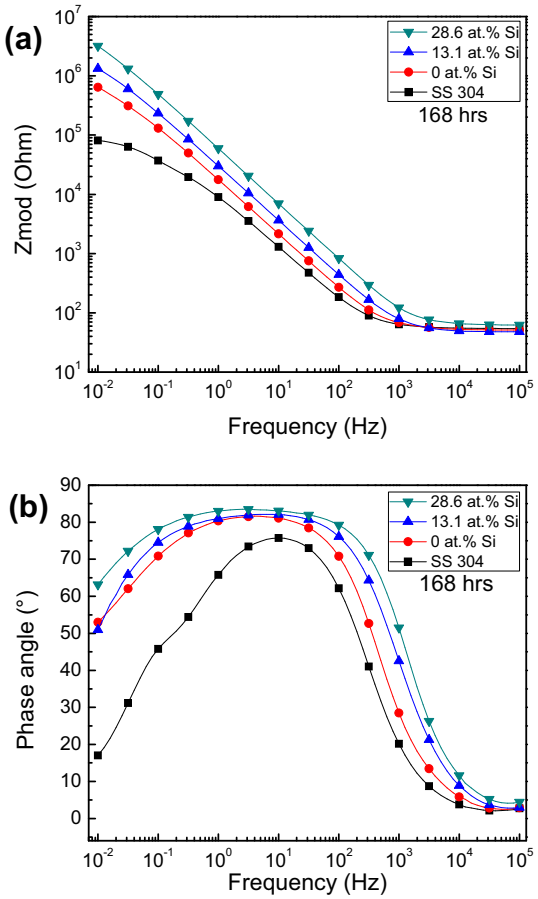

Fig. 7 **a** Impedance modulus (Zmod), and **b** phase angle after 168 h of immersion for the NbN films having different Si concentrations and the SS 304

present in PVD thin films [27, 29, 38, 52, 53]. Hence, it can be concluded that the coated specimens with high Si concentration are in the passive state, while the stainless steel 304, which has a short relaxation time, shows an active behavior.

The EIS spectra were fitted using the Simplex algorithm to obtain the best possible fitting (minimum figure of merit). For all the EIS data, a Kramers–Kroning analysis was performed to confirm the validity of the measurements before proceeding with the equivalent circuit analysis. The impedance spectra of the coated specimens displayed in Fig. 6 were analyzed using the electric circuit (EC) model shown in Fig. 8, where $R_{\text{electrolyte}}$ represents the solution resistance; R_{pore} represents the thin-film resistance; $R_{\text{interface}}$ represents the interface resistance; C_{thinfilm} represents a constant phase element for the thin film; and $C_{\text{interface}}$ represents a constant phase element for the interface between the substrate and the coating. The capacitances (C_{thinfilm} and $C_{\text{interface}}$) are simulated using a constant phase element (CPE), where the indexes n and m can vary from 0.5 to 1; ideally, a value of 1 represents a perfect capacitor. This EC has been effectively used to represent coatings with a long relaxation time behavior [27, 30, 52–56], and also stainless steels due to the passive oxide layer of its surface [33, 35, 52]. There was no need to use a different circuit for any of the samples, as can be observed in Fig. 6, where the continuous line corresponds to the fitting results and the symbol to the measurement data.

The simulation results from the EC after 168 h immersion time are shown in Table 3. When n and m approach 1, the CPEs (capacitors) presented a fully capacitive behavior, which means that the coatings are basically free of microporosities and have better corrosion resistance. At low frequencies, the CPEs behave as an open circuit, while at high frequencies they behave as a short circuit. The simulation allows one to estimate the polarization resistance (PR), which is a measure of the corrosion resistance provided by the coating, and it is calculated by adding $R_{\text{interface}} + R_{\text{pore}}$ [54, 57–59]; higher PR values mean a larger protective capability. The variation in PR as a function of time and Si concentration is plotted in Fig. 9. The value of PR for the SS 304 is one order of magnitude lower than for the films in agreement with both the potentiodynamic polarization corrosion potential and the lower modulus of impedance. Moreover, it decreased slightly as a function of time, indicating that the electrolyte is attacking the SS 304 surface. This can be observed in Fig. 10a that shows the SEM image after the 168 h of immersion; many (arrows in the figure) localized corrosion defects (pitting sites) are observed on the SS 304 surface, besides the accumulation of some salt crystals. On the other hand, the PR value for the NbN film is one order of magnitude larger than SS 304 and it barely changes with the immersion time. Comparatively, the SEM image (Fig. 10b) shows a lower density of corrosion defects, although some of them are larger than for the SS 304, probably related to delamination of the NbN film around the corrosion defect. Such result is in agreement with the slight variations observed in the phase angle (Fig. 6d) for the NbN films, which suggest that even without polarization, the electrolyte is creating some modifications of the films surface. A small improvement in the PR value was observed for the $Nb_xSi_yN_z$ sample with 13.1 at.% of Si, where the PR value was nearly constant in time, as the impedance spectra, and very few small corrosion defects are observed in Fig. 10c. Finally, the $Nb_xSi_yN_z$ film with

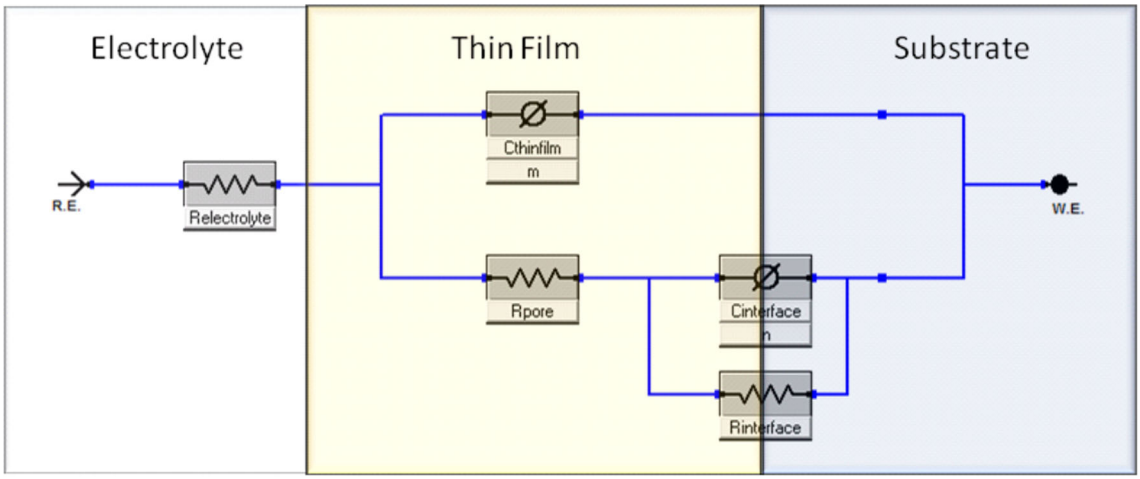

Fig. 8 Equivalent electric circuit used for the simulation of the impedance spectra; reference electrode (RE); working electrode (WE)

Table 3 Simulation results from EIS measurements after 168-h immersion time

Sample name	Silicon (at.%)	$R_{electrolyte}$ (Ω)	$R_{interface}$ (Ω)	R_{pore} (Ω)	$C_{interface}$ ($S*s^n$)	n	$C_{thinfilm}$ ($S*s^m$)	m
SS 304	0	54	8.1E4	2.6E4	3E−5	0.629	1.9E−5	0.890
NbN-0Si	0	51	6.4E5	6.7E5	2E−5	1	1E−5	0.909
NbN-12Si	13.1	44	1.5E6	1.5E6	5.6E−6	0.842	4.5E−6	0.924
NbN-17Si	28.6	62	3.1E6	5.7E6	3.8E−6	1	3.1E−6	0.925

N and m can vary from 0.5 to 1, and a value of 1 represents a perfect capacitor

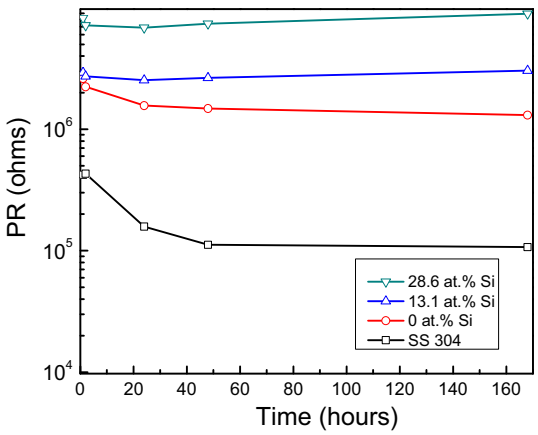

Fig. 9 Variation in the polarization resistance (PR) of the NbN and NbN-Si films in comparison with the SS 304 substrate after 1, 24, 48, and 168 h of immersion in the NaCl solution

the maximum Si content (28.6 at.%) has a PR value nearly two orders of magnitude higher than the substrate, it remained perfectly stable with the immersion time, and no corrosion defects were observed in the SEM image after the 168 h of immersion. The overall results indicated that the PR value increased as the Si content was increased and the film structure changed from crystalline to amorphous; the initiation of the localized corrosion defects is delayed or limited as the Si content increased, probably due to modification in the electronic configuration [34] or due to a modification in the original porosity of the NbN films as Si is added [60].

In summary, the hardness of the films is higher than that of the SS 304. The films are able to protect the SS 304 from corrosion, as was supported by the SEM images, and the potentiodynamic polarization curves revealed that the film with the highest Si concentration has the lowest corrosion rate. Moreover, the polarization resistance obtained from the EIS measurements suggests that the addition of Si improves the barrier properties of the coatings. The corrosion resistance likely increased due to the disappearance of grain boundaries, since the film structure at a high Si concentration becomes amorphous. Such compact $Nb_xSi_yN_z$ amorphous films drastically reduce the diffusion paths for the electrolyte and improve the corrosion resistance of the coated substrates. Therefore, the amorphous films produced in this study can be used to protect the SS 304 from corrosion while maintaining high hardness.

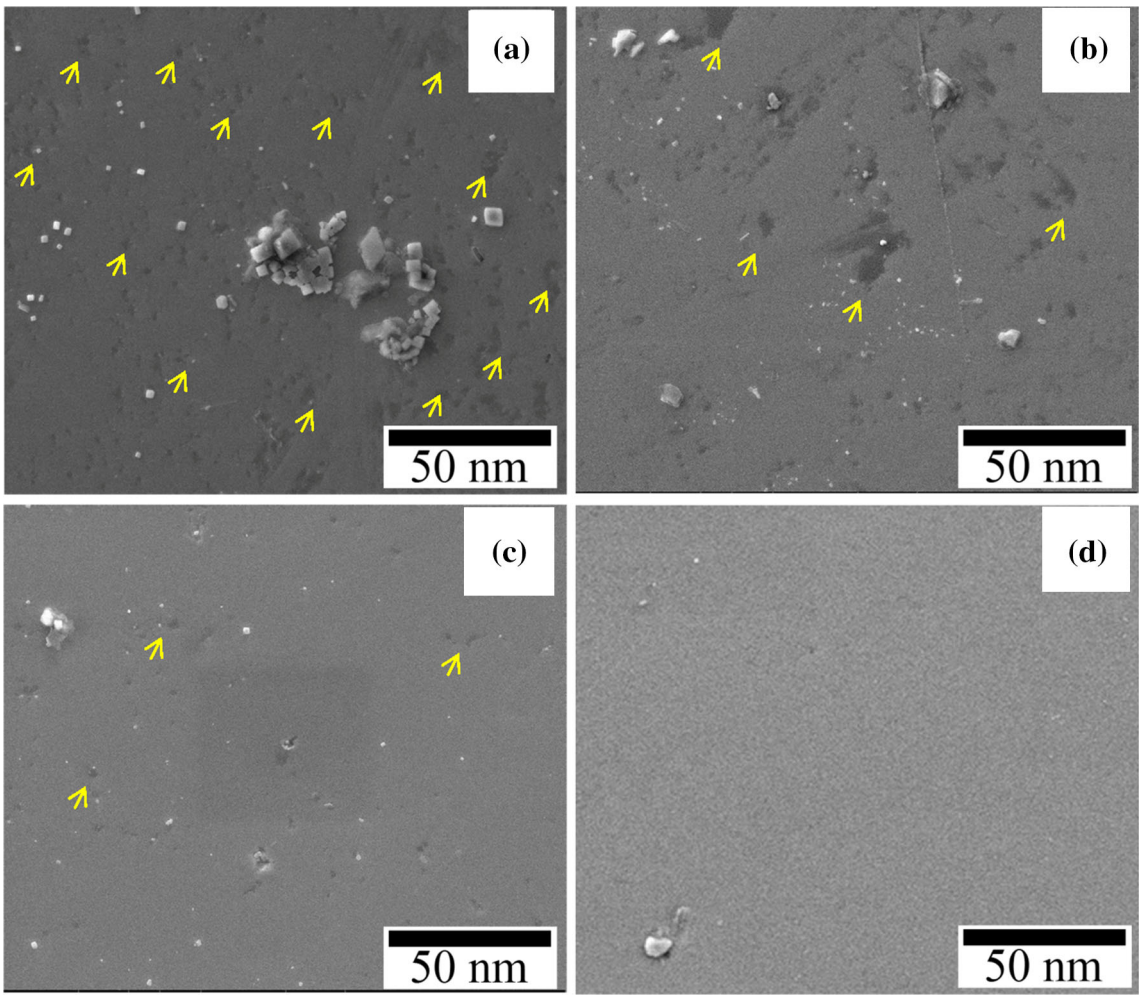

Fig. 10 Representative SEM surface images showing the surface areas exposed to the NaCl electrolyte after 168 h of immersion; **a** SS 304, **b** film with 0 at.% Si, **c** film with 13.1 at.% Si, and **d** film with 28.6 at.% Si

4 Conclusions

The addition of square Si pieces onto the racetrack of a Nb target allowed us to co-deposit $Nb_xSi_yN_z$ thin films and achieve a high Si concentration.

The elemental analysis by XPS confirmed the presence of both Si_3N_4 and NbN phases, while XRD confirmed that no crystalline Si_3N_4 phase was present and that there was formation of the cubic NbN phase with small grain sizes. The a-Si_3N_4 phase can be at the grain boundaries of the NbN grains and prevent their growth.

The sputtered Si-doped thin films showed a decrease in hardness compared to the sputtered NbN film, but still the hardness of the films is much higher than that of the SS 304.

The analysis of the electrochemical response of the $Nb_xSi_yN_z$ films as a function of the immersion time suggests that the addition of Si led to an improvement in the barrier properties of the films, protecting the stainless steel from corrosion. Moreover, there was a linear increase in the polarization resistance as a function of Si content. The amorphization observed by the XRD analysis and the high hardness shows that is possible to synthesize amorphous Si-rich $Nb_xSi_yN_z$ films to improved corrosion resistance.

Acknowledgments This research was carried out with financial support from DIB-Universidad Nacional de Colombia. The authors acknowledged L. Huerta for XPS measurements and H. Zarco for technical assistance, both at the IIM-UNAM. SER acknowledges financial support from DGAPA-PAPIIT projects.

References

1. S. Veprek, M.G.J. Veprek-Heijman, P. Karvankova, J. Prochazka, Thin Solid Films **476**, 1 (2005)
2. A. Vyas, Y.H. Lu, Y.G. Shen, Surf. Coat. Technol. **204**, 1528 (2010)
3. Q. Yang, F. Cai, L.R. Zhao, X. Huang, Surf. Coat. Technol. **203**, 606 (2008)

4. R.F. Bunshah, *Handbook of Hard Coatings: Wear and Corrosion Resistant Hard Coatings for Non-cutting Tool Applications* (Noyes Publications, Park Ridge, N.J., 2001)
5. R.L. Li, J.P. Tu, C.F. Hong, D.G. Liu, H.L. Sun, Surf. Coat. Technol. **204**, 470 (2009)
6. A. Kumar, D. Kaur, Surf. Coat. Technol. **204**, 1132 (2009)
7. P.J. Kelly, R.D. Arnell, Vacuum **56**, 159 (2000)
8. S. Karthikeyan, A.E. Hill, J.S. Cowpe, R.D. Pilkington, Vacuum **85**, 634 (2010)
9. I. Safi, Surf. Coat. Technol. **127**, 203 (2000)
10. H.Y. Lee, W.S. Jung, J.G. Han, S.M. Seo, J.H. Kim, Y.H. Bae, Surf. Coat. Technol. **200**, 1026 (2005)
11. M. Benkahoul, P. Robin, S.C. Gujrathi, L. Martinu, J.E. Klemberg-Sapieha, Surf. Coat. Technol. **202**, 3975 (2008)
12. H.-H. Lin, C.-C. Chou, J.-W. Lee, Thin Solid Films **518**, 7509 (2010)
13. H.N. Shah, R. Jayaganthan, D. Kaur, Appl. Surf. Sci. **257**, 5535 (2011)
14. H.N. Shah, R. Jayaganthan, A.C. Pandey, Mater. Des. **32**, 2628 (2011)
15. E. Bousser, M. Benkahoul, L. Martinu, J.E. Klemberg-Sapieha, Surf. Coat. Technol. **203**, 776 (2008)
16. X.Z. Ding, X.T. Zeng, Y.C. Liu, Q. Yang, L.R. Zhao, Vac. Sci. Technol **A22**, 2351 (2004)
17. E. Ribeiro, L. Rebouta, S. Carvalho, F. Vaz, G.G. Fuentes, R. Rodriguez, M. Zazpe, E. Alves, P. Goudeau, J.P. Rivière, Surf. Coat. Technol. **188–189**, 351 (2004)
18. S. Veprek, Surf. Coat. Technol. **97**, 15 (1997)
19. T. Fu, Z.F. Zhou, K.Y. Li, Y.G. Shen, Mater. Lett. **59**, 618 (2005)
20. T. Fu, Z.F. Zhou, K.Y. Li, Y.G. Shen, Surf. Coat. Technol. **200**, 2525 (2005)
21. T. Fu, Y.G. Shen, Z.F. Zhou, K.Y. Li, Mater. Sci. Eng. B **123**, 158 (2005)
22. Y. Dong, Y. Liu, J. Dai, G. Li, Appl. Surf. Sci. **252**, 5215 (2006)
23. J. Wang, Z. Song, K. Xu, Surf. Coat. Technol. **201**, 4931 (2007)
24. Z.X. Song, Y. Wang, C.J.F. Wang, C.L. Liu, K.W. Xu, Surf. Coat. Technol. **201**, 5412 (2007)
25. C.S. Sandu, M. Benkahoul, R. Sanjinés, F. Lévy, Surf. Coat. Technol. **201**, 2897 (2006)
26. T. Murakami, S. Sasaki, K. Ichikawa, A. Kitahara, Intermetallics **9**, 621 (2001)
27. Y.H. Yoo, J.H. Hong, J.G. Kim, H.Y. Lee, J.G. Han, Surf. Coat. Technol. **201**, 9518 (2007)
28. G. Ramírez, S.E. Rodil, S. Muhl, D. Turcio-Ortega, J.J. Olaya, M. Rivera, E. Camps, L. Escobar-Alarcón, J. Non-Cryst. Solids **356**, 2714 (2010)
29. J.J. Olaya, S.E. Rodil, S. Muhl, E. Sánchez, Thin Solid Films **474**, 119 (2005)
30. D. Turcio-Ortega, S.E. Rodil, S. Muhl, Diam. Relat. Mater. **18**, 1360 (2009)
31. J.F. Flores, J.J. Olaya, R. Colás, S.E. Rodil, B.S. Valdez, I.G. Fuente, Corros. Eng. Sci. Technol. **41**, 168 (2006)
32. J.J. Olaya, G. Wei, S.E. Rodil, S. Muhl, B. Bhushan, Vacuum **81**, 610 (2007)
33. G. Ramírez, S.E. Rodil, H. Arzate, S. Muhl, J.J. Olaya, Appl. Surf. Sci. **257**, 2555 (2011)
34. G. Ramírez, D. Oezer, M. Rivera, S.E. Rodil, R. Sanjinés, Thin Solid Films **558**, 104 (2014)
35. M. Flores, L. Huerta, R. Escamilla, E. Andrade, S. Muhl, Appl. Surf. Sci. **253**, 7192 (2007)
36. D.M. Marulanda, J.J. Olaya, U. Piratoba, A. Mariño, E. Camps, Thin Solid Films **519**, 1886 (2011)
37. S.E. Rodil, J.J. Olaya, S. Muhl, B. Bhushan, G. Wei, Surf. Coat. Technol. **201**, 6117 (2007)
38. J.J. Olaya, S.E. Rodil, S. Muhl, Thin Solid Films **516**, 8319 (2008)
39. N. Jiang, Y.G. Shen, Y.W. Mai, T. Chan, S.C. Tung, Mater. Sci. Eng. B **106**, 163 (2004)
40. M. Fenker, M. Balzer, R.V. Büchi, H.A. Jehn, H. Kappl, J.J. Lee, Surf. Coat. Technol. **163–164**, 169 (2003)
41. J.J. Jeong, C.M. Lee, Appl. Surf. Sci. **214**, 11 (2003)
42. G. Jouve, C. Séverac, S. Cantacuzène, Thin Solid Films **287**, 146 (1996)
43. C. Louro, A. Cavaleiro, F. Montemor, Surf. Coat. Technol. **142–144**, 964 (2001)
44. M. Diserens, J. Patscheider, F. Lévy, Surf. Coat. Technol. **108–109**, 241 (1998)
45. A. Cavaleiro, J.T.M. de Hosson, *Nanostructured Coatings* (Springer, New York, 2006)
46. M. Benkahoul, C.S. Sandu, N. Tabet, M. Parlinska-Wojtan, A. Karimi, F. Lévy, Surf. Coat. Technol. **188–189**, 435 (2004)
47. S. Zhang, N. Ali, *Nanocomposite Thin Films and Coatings: Processing, Properties and Performance* (Imperial College Press, London, 2007)
48. C. Suryanarayana, M.G. Norton, *X-ray Diffraction: A Practical Approach* (Springer, US, 1998)
49. S. Veprek, A. Niederhofer, K. Moto, T. Bolom, H.D. Männling, P. Nesladek, G. Dollinger, A. Bergmaier, Surf. Coat. Technol. **133–134**, 152 (2000)
50. S. Veprek, S. Reiprich, Thin Solid Films **268**, 64 (1995)
51. A. Lupinacci, K. Chen, Y. Li, M. Kunz, Z. Jiao, G.S. Was, M.D. Abad, A.M. Minor, P. Hosemann, J. Nucl. Mater. **458**, 70 (2015)
52. C. Liu, Q. Bi, A. Leyland, A. Matthews, Corros. Sci. **45**, 1243 (2003)
53. C. Liu, Q. Bi, A. Leyland, A. Matthews, Corros. Sci. **45**, 1257 (2003)
54. S.H. Ahn, Y.S. Choi, J.G. Kim, J.G. Han, Surf. Coat. Technol. **150**, 319 (2002)
55. V.K. William Grips, H.C. Barshilia, V.E. Selvi, Kalavati, K.S. Rajam, Thin Solid Films **514**, 204 (2006)
56. R. Bayón, A. Igartua, X. Fernández, R. Martínez, R.J. Rodríguez, J.A. García, A. de Frutos, M.A. Arenas, J. de Damborenea, Tribol. Int. **42**, 591 (2009)
57. D.K. Merl, P. Panjan, M. Cekada, M. Macek, Electrochim. Acta **49**, 1527 (2004)
58. K.L. Chang, S. Han, J.H. Lin, J.W. Hus, H.C. Shih, Surf. Coat. Technol. **172**, 72 (2003)
59. S.H. Ahn, J.H. Lee, H.G. Kim, J.G. Kim, Appl. Surf. Sci. **233**, 105 (2004)
60. K.-L. Chang, S.-C. Chung, S.-H. Lai, H.-C. Shih, Appl. Surf. Sci. **236**, 406 (2004)